Enhanced Third-Order Optical Nonlinearity Driven by Surface-Plasmon Field Gradients

Vasily Kravtsov, Sultan AlMutairi, Ronald Ulbricht, A. Ryan Kutayiah, Alexey Belyanin, and Markus B. Raschke

Phys. Rev. Lett. **120**, 203903 — Published 18 May 2018

DOI: 10.1103/PhysRevLett.120.203903

Enhanced third-order optical nonlinearity driven by surface-plasmon field gradients

Vasily Kravtsov,[1] Sultan AlMutairi,[2] Ronald Ulbricht,[1] A. Ryan Kutayiah,[2] Alexey Belyanin,[2] and Markus B. Raschke[1,*]

[1]*Department of Physics, Department of Chemistry, and JILA, University of Colorado, Boulder, CO, 80309, USA*

[2]*Department of Physics and Astronomy, Texas A&M University, College Station, TX, 77843, USA*

(Dated: May 4, 2018)

Abstract

Efficient nonlinear optical frequency mixing in small volumes is key for future on-chip photonic devices. However, the generally low conversion efficiency severely limits miniaturization to nanoscale dimensions. Here we demonstrate that gradient-field effects can provide for an efficient, conventionally dipole-forbidden nonlinear response. We show that a *longitudinal* nonlinear source current can dominate the third-order optical nonlinearity of the free electron response in gold in the technologically important near-IR frequency range where the nonlinearities due to other mechanisms are particularly small. Using adiabatic nanofocusing to spatially confine the excitation fields, from measurements of the $2\omega_1 - \omega_2$ four-wave mixing response as a function of detuning $\omega_1 - \omega_2$, we find up to 10^{-5} conversion efficiency with a gradient field contribution to $\chi^{(3)}_{\mathrm{Au}}$ of up to 10^{-19} $\mathrm{m}^2/\mathrm{V}^2$. The results are in good agreement with theory based on plasma hydrodynamics and underlying electron dynamics. The associated increase in nonlinear conversion efficiency with decreasing sample size, which can even overcompensate the volume decrease, offers a new approach for enhanced nonlinear nano-optics. This will enable more efficient nonlinear optical devices and the extension of coherent multidimensional spectroscopies to the nanoscale.

* Corresponding author: markus.raschke@colorado.edu

Nonlinear optics provides for optical frequency conversion and all-optical information processing that can potentially overcome speed limitations of modern electronics and enable faster computing and data communication. Device miniaturization and on-chip integration thus require an efficient nonlinear optical response in deep sub-wavelength volumes.

However, because intrinsic optical nonlinearities are generally weak, various approaches to achieve enhanced nonlinear conversion efficiencies have been considered, from exploring materials with high nonlinearities [1] to optimizing the driving field distribution [2]. Simultaneous mode volume compression and local field engineering for enhanced nonlinear optics can be achieved through photonic crystals [3], metamaterials [4], microcavities [5], structures with reduced speed of light [6], or plasmon-resonant metallic nanoparticles [7].

A significant gain in third-order nonlinear efficiency is of particular interest as it allows for all-optical switching, femtosecond pulse control, and coherent ultrafast spectroscopy via four-wave mixing (FWM) [8–11]. On the nanoscale [12, 13], third-order effects have been discussed in terms of plasmonic local field enhancement [14–22], or in graphene due to the associated extreme spatial field confinement [23], with some attention to finite size effects [24–26], surface contribution [27], or ponderomotive terms [28].

Here we demonstrate a new mechanism of the third-order optical nonlinearity in metallic nanoparticles and nanoantennas. The mechanism is based on large longitudinal field gradients associated with strongly confined plasmonic fields. While radiation of the associated longitudinal nonlinear currents into propagating transverse far-field waves is forbidden for translationally invariant bulk metal, this restriction is relaxed on the nanoscale. We find that in subwavelength structures the gradient field mechanism becomes an efficient and even dominant source term in FWM. Using plasmonic nanofocusing to spatially confine the excitation fields, we show that the corresponding third-order nonlinear optical susceptibility $\chi^{(3)}$ in the near-IR spectral range can be enhanced > 5 times when transitioning from non-degenerate to degenerate FWM with up to 10^{-5} conversion efficiency and a corresponding contribution to $\chi^{(3)}_{\mathrm{Au}}$ of up to 10^{-19} $\mathrm{m}^2/\mathrm{V}^2$. We further implement a plasma hydrodynamic model that provides even semi-quantitative description of the nonlinear conversion efficiency and underlying electron dynamics.

In the experiment, we measure the FWM signal generated in a Au nano-tip antenna with $\sim$10 nm apex radius as a generalized model structure. In order to spatially confine the excitation fields and eliminate unspecific background we use adiabatic nanofocusing and spatially filtered tip apex emission detection as shown in Fig. 1a. Incident light is grating-coupled into surface plasmon

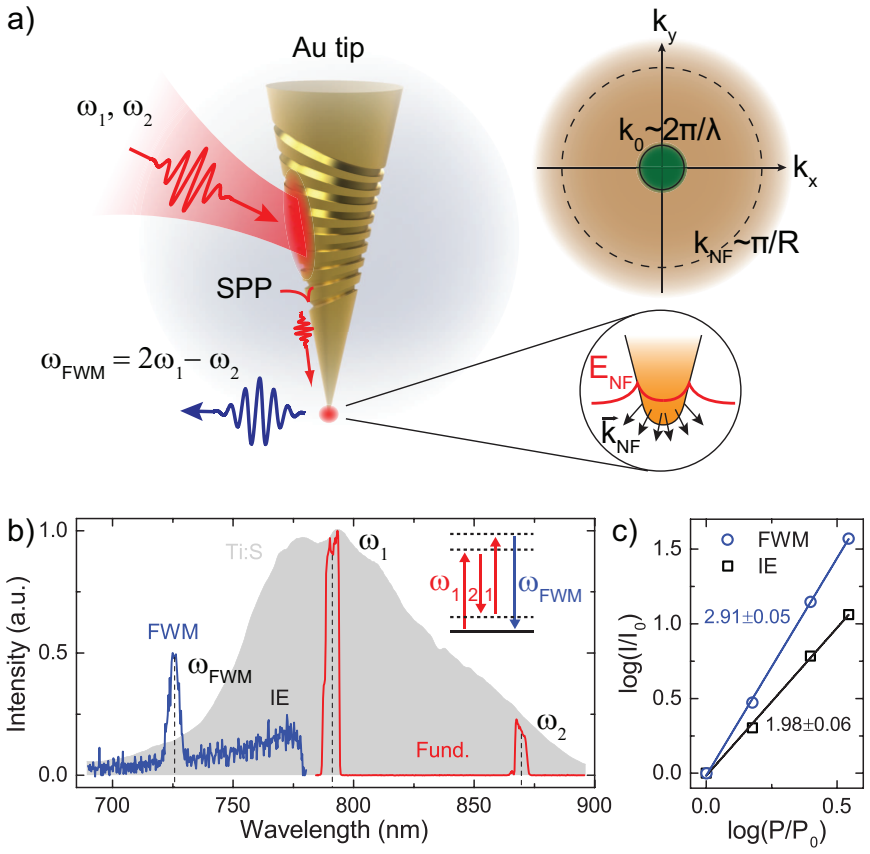

FIG. 1. (a) Experimental configuration (left), with enhanced efficiency due to broad distribution of field momenta $k_{x,y}$ for nanofocused SPPs associated with gradient field and spatial confinement (right). (b) Full laser spectrum (gray), fundamental scattering off the tip apex (red), incoherent emission (IE) background, and coherent FWM peak (blue). (c) Power dependence of the FWM signal (blue) and incoherent emission (black) showing cubic and quadratic dependence, respectively.

polaritons (SPPs) that propagate toward the tip apex, adiabatically compress with accompanying field enhancement, and generate a nonlinear optical response predominantly in the nanoscopic apex volume [33].

As shown in Fig. 1b, two spectrally narrow pump pulses at center frequencies ω_1 and ω_2 (red) and full width at half maximum (FWHM) of 10 nm are derived from a Ti:Sapphire oscillator (Femtolasers, 10 fs nominal pulse duration, $\sim$ 800 nm, spectrum shown in gray). ω_1 and ω_2 are obtained by blocking parts of the original spectrum with a tunable hardware amplitude mask in the Fourier plane of a $4f$ pulse shaper (using a CRi SLM640). Spectral phase and amplitude are controlled to obtain a flat spectral phase across the full bandwidth of the optical field at the tip apex by performing multiphoton intrapulse interference phase scans (MIIPS) based on apex-generated

second harmonic generation as feedback signal [33].

The FWM emission (Fig. 1b, blue) from the tip apex is spatially filtered and detected with a spectrometer (Princeton Instruments). For reference, we measure FWM on a flat single-crystalline Au surface in far-field under normal incidence and back-reflection detection.

In addition to FWM, a spectrally broad background is observed due to incoherent emission (IE) from electronic excitations within the *sp*-band of Au [34]. Its power dependence is quadratic (1.98 ± 0.06) as shown in Fig. 1c (black) and exhibits a frequency-dependent power law exponent due to varying spectral shape (see Supplement), in agreement with previous studies [34, 35].

The coherent nonlinear FWM signal is centered at $\omega_{\mathrm{FWM}} = 2\omega_1 - \omega_2$. Its power dependence is close to cubic (2.91 ± 0.05) as shown in Fig. 1c (blue) and depends quadratically and linearly on the

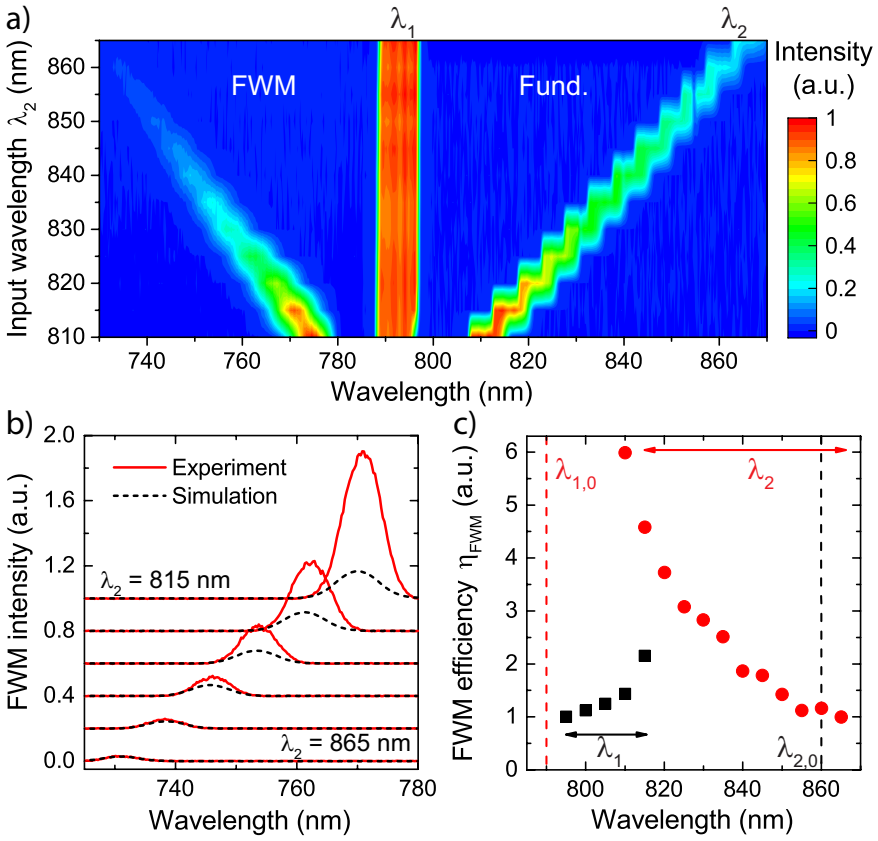

FIG. 2. Measurement of the FWM efficiency: (a) FWM (left) and fundamental (right) tip-scattered spectra collected for varying excitation wavelength, (b) experimental FWM spectra for selected excitation wavelengths (red solid, $\lambda_1 = 790$ nm, $\lambda_2 = 815$, 825, 835, 845, 855, and 865 nm) together with calculated reference signal (black dashed), (c) FWM efficiency extracted in two experiments where either $\lambda_{1,0}$ (red) or $\lambda_{2,0}$ (black) are held constant, while varying λ_2 and λ_1, respectively.

incident intensities at ω_1 and ω_2, respectively, as expected. With the estimated field enhancement at the apex of ~ 25 and the resulting peak electric field of $\sim 5 \cdot 10^9$ V/m, the nano-FWM conversion efficiency [10] reaches $\sim 10^{-5}$.

In order to investigate the mechanism underlying this large FWM generation efficiency, we then measure the spectral dependence of the FWM response. As shown in Fig. 2a, we collect FWM (left) and fundamental (right) spectra emitted from the tip apex for excitation with constant frequency ω_1, while varying ω_2. Reference FWM spectra are calculated from integration over the fundamental scattering spectrum at the tip apex $I(\omega)$, assuming a flat spectral phase and frequency-independent third-order susceptibility. The resulting expected $I_{ref}(\omega)$ is

$$I_{ref}(\omega) \propto \left| \iiint_{-\infty}^{\infty} d\omega_{1,2,3} \sqrt{I(\omega_1)I(\omega_2)I(\omega_3)}\, \delta(\omega - \omega_1 + \omega_2 - \omega_3) \right|^2, \quad (1)$$

plotted in Fig. 2b (black dashed) together with the experimental data (red solid) for selected values of ω_2. While peak position and overall spectral shape are in good agreement, the measured FWM intensity increasingly exceeds the reference values calculated from Eq. 1 as ω_2 approaches ω_1. We quantify that increase by calculating the FWM efficiency η_{FWM} as the ratio between the tip I_{FWM} and reference I_{ref} FWM signals $\eta_{FWM} = I_{FWM}/I_{ref}$. η_{FWM} is plotted in Fig. 2c (red circles) as a function of the varied excitation wavelength λ_2, and exhibits a 6-fold increase within the spectral range of the measurement. We then perform a corresponding measurement with variable λ_1 for fixed λ_2 (black squares) exhibiting an apparent opposite trend. However, when plotting both datasets against the detuning $\delta\omega = \omega_1 - \omega_2$ as shown in Fig. 3a, the FWM efficiency shows a universal increase with decreasing $\delta\omega$ for both measurements (red and black open symbols, left scale). This indicates that the FWM mechanism is independent of the excitation frequency, and only depends on detuning. The behavior is general, with a similar behavior of the FWM response observed for Au nanorods (see Supplement). For comparison, the corresponding FWM result for a flat single-crystalline Au surface measured in far-field is shown in Fig. 3a (filled blue squares), with efficiency that is low and independent on detuning $\delta\omega$.

In general, the third-order polarization $P^{(3)}(\omega_{FWM})$ can be frequency-dependent through $\chi^{(3)}(\omega)$, local field enhancement factors at excitation and FWM frequencies $L(\omega), L(\omega_{FWM})$, and excitation spectrum $E(\omega)$, with $P^{(3)}(\omega_{FWM}) \sim L(\omega_{FWM})\chi^{(3)}(\omega)L^3(\omega)E^3(\omega)$. In our case, all factors corresponding to the local fields at the excitation frequencies are contained in both measured I_{FWM} and calculated reference I_{ref} FWM intensities due to the spatially localized apex detection, and therefore cancel out for the calculated FWM efficiency $\eta_{FWM} = I_{FWM}/I_{ref}$ (for

details, see Supplement and [36]). Further, under off-resonant near 1.5 eV excitation, $L(\omega_{\mathrm{FWM}})$ varies only weakly across the narrow experimental range of FWM frequencies. Therefore the FWM efficiency is expected to follow the spectral behavior of the nonlinear susceptibility itself $\eta_{\mathrm{FWM}}(\omega) \propto \left[\chi^{(3)}(\omega;\omega_1,\omega_1,-\omega_2)\right]^2$.

For bulk Au, $\chi^{(3)}$ is weak in general with limited contributions from hot-electron, intraband, and interband terms [37]. The hot-electron contributions only become significant for pulse durations comparable to or exceeding the electron gas thermalization time of ~ 500 fs and for excitation wavelength close to the *d*- to *sp*-band transition [37, 38]; they are therefore expected to be negligible in our case (< 100 fs, ~ 1.5 eV). Further, the *sp*-band in Au is very close to parabolic, implying zero restoring force and vanishing intraband nonlinearity in the dipole approximation [37]. Additional higher-order magnetic-dipole and electric-quadrupole contributions are longitudinal and do not out-couple into transverse radiating modes. The dominant contribution to the nonlinearity of bulk Au is then expected to involve either two-photon resonant or one-photon off-resonant *interband* electronic transitions between *d*- and *sp*-bands of Au [10]. The observed weak depen-

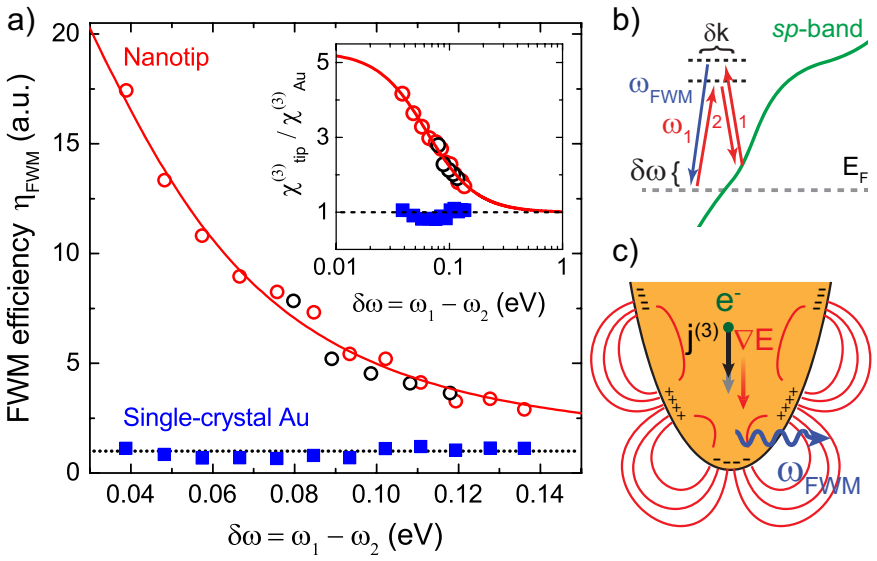

FIG. 3. Modeling the FWM efficiency: (a) experimental result for nano-tip (red and black open circles) and single-crystalline Au surface in far-field (filled blue squares, dotted line is a guide to the eye), together with the model fit (red). Inset shows the enhancement of the third-order susceptibility of the tip relative to that of bulk Au as a function of detuning between the two excitation frequencies. (b) Schematic of the intraband FWM process. (c) Illustration of the FWM generated by longitudinal nonlinear currents and out-coupled into transverse fields.

dence of the FWM efficiency on detuning $\delta\omega$ in bulk Au shown in Fig. 3a (blue squares) is then consistent with the absence of resonant behavior in $\delta\omega$ for such transitions.

In nanostructures, in contrast, the *intraband* contribution can become an efficient and leading source term. Spatially compressed SPP modes at the tip apex $E = E_0 e^{i\mathbf{k}_{\mathrm{NF}}\cdot\mathbf{r}}$ exhibit strong field gradients $|\partial E/\partial \mathbf{r}| \propto k_{\mathrm{NF}} E$ in both transverse and longitudinal directions, corresponding to large linear momenta $p_{\mathrm{NF}} = \hbar k_{\mathrm{NF}} \sim \pi\hbar/R$, where R is the tip apex radius. For typical radii of $R \sim 10$ nm the near-field momenta can reach beyond $k_{\mathrm{NF}} \sim 3 \cdot 10^6$ cm^{-1}, exceeding the corresponding far-field value for the given wavelength range by 2 orders of magnitude. These in-plane momenta then allow for resonant and phase-matched electronic transitions within the *sp*-band as illustrated in Fig. 3b. With the apex-confined field parallel with respect to the tip axis, the dominant component of the third-order nonlinear source current $\mathbf{j}^{(3)}$ is longitudinal. This gives rise to FWM emission or scattering with primarily dipolar characteristics as given by the antenna mode of the tip, with maximum radial emission, and zero emission in the axial direction [30, 39]. This facilitates outcoupling of the longitudinal current oscillations and resulting polarization density to the outgoing transverse electromagnetic waves as pictured in Fig. 3c. This is in fundamental contrast to the case of bulk Au, where the corresponding radiative process is forbidden for far-field reflection or refraction in translationally invariant media.

To provide a simple model to quantify the nonlinear response of the free electrons in a nanostructure (see Supplement for details), we consider the equation of motion for a degenerate electron plasma against the neutralizing background of immobile ions, neglecting the thermal motion, given by

$$\frac{\partial \mathbf{v}}{\partial t} + \gamma \cdot \mathbf{v} + (\mathbf{v}\cdot\nabla)\,\mathbf{v} - \frac{e}{m_e}\mathbf{E} - \frac{e}{m_e c}\mathbf{v}\times\mathbf{B} = 0, \tag{2}$$

with external electric and magnetic fields $\mathbf{E}$ and $\mathbf{B}$, electron velocity $\mathbf{v}$, effective mass m_e, electron charge e, and collision rate γ. We then consider longitudinal components of the velocity perturbation, fields, and their gradients along the x axis, $\mathbf{E} = E\hat{x}$ and $\mathbf{v} = \mathrm{v}\hat{x}$, and neglect the contribution from the magnetic field. We treat the electric field as a perturbation, approximate field gradients ∂_x by $1/R$, and find the third-order nonlinear term in the electron velocity $\mathrm{v}^{(3)}$ at frequency $\omega_3 = 2\omega_1 - \omega_2$ in response to the two pump fields E_1 and E_2 at frequencies ω_1 and ω_2.

The third-order susceptibility is related to the velocity through the nonlinear polarization $P^{(3)} =$

$\chi^{(3)}E_1^2E_2^*e^{-i\omega_3 t}$ and current density $j^{(3)} = \dfrac{dP^{(3)}}{dt} = en^{(0)}\mathrm{v}^{(3)}$, and can be expressed as

$$\chi^{(3)}_{\mathrm{intra}} = i\frac{6n^{(0)}e^4}{\omega_3 m_e^3 R^2}\frac{\gamma}{(\gamma - i\omega_1)^2(\gamma + i\omega_2)(\gamma - i\omega_3)\left(\gamma^2 + \delta\omega^2\right)}, \tag{3}$$

with the electron density $n^{(0)}$ and a resonance at $\omega_1 = \omega_2$ with a Lorentzian FWHM of 2γ. A fit of this model to our experimental $\eta_{\mathrm{FWM}}(\delta\omega) \propto \left(\chi^{(3)}_{\mathrm{Au}} + \chi^{(3)}_{\mathrm{intra}}(\delta\omega)\right)^2$, with γ and $\chi^{(3)}_{\mathrm{intra}}(0)$ as the only free parameters, is in excellent agreement with our experimental data (Fig. 3a, red solid line). The resulting value of $2\gamma = 128 \pm 14$ meV corresponds to the electron collision rate of $\gamma = 64 \pm 7$ meV, or scattering time $\tau = 10.3 \pm 1.2$ fs, which is in good agreement with the Drude relaxation time of $\tau_{\mathrm{D}} = 9 - 14$ fs for Au [40, 41].

From the fit value $\chi^{(3)}_{\mathrm{intra}}(0)$, we obtain the ratio of the intraband contribution at zero detuning to the third-order susceptibility of bulk Au, with $\chi^{(3)}_{\mathrm{intra}}(0)/\chi^{(3)}_{\mathrm{Au}} = 4.3$. According to Eq. 3, this parameter depends on the radius of curvature at the tip apex R. The frequency dependence of the relative contribution of the gradient-induced nonlinearity is shown in the inset of Fig. 3a, with the black dashed line indicating the intrinsic third-order susceptibility of Au as extracted from the far-field measurement on the single-crystal Au sample. Indeed, for tips of different sharpness, we extract values of $\chi^{(3)}_{\mathrm{intra}}(0)/\chi^{(3)}_{\mathrm{Au}} = 2.2 - 8.7$ and $\gamma = 34 - 69$ meV, with the distribution reflecting the expected range of tip apex radii and damping to a good approximation (see Supplement). We note that, as the shape of the tip apex deviates from a perfect sphere, slight variations in geometry effectively correspond to variation in the sphere radius in the model.

We then estimate the absolute value of the third-order nonlinear susceptibility assuming all frequencies $\omega_{1,2,3} \sim 1.5$ eV, carrier density $n^{(0)} \sim 6 \times 10^{22}$ cm^{-3}, m_e equal to the effective electron mass in Au, and tip apex diameter $2R \sim 15$ nm:

$$|\chi^{(3)}| \sim \frac{6n^{(0)}e^4}{m_e \gamma R^2 \omega_1^2 \omega_2 \omega_3^2} \sim 7.6 \times 10^{-12}\ \mathrm{esu}. \tag{4}$$

This corresponds to $|\chi^{(3)}| \sim 1.1 \times 10^{-19}$ m^2/V^2 in SI units, and agrees with a previously reported value for Au of $2 \cdot 10^{-19}$ m^2/V^2 [42] for similar excitation conditions.

Lastly, within the limits given by damage threshold and minimum necessary signal level, we measure coherent FWM efficiency together with the incoherent nonlinear emission for selected values of excitation power, with the results shown in Fig. 4a. Our measured incoherent emission spectra undergo a significant transformation with increasing incident power. Although the exact

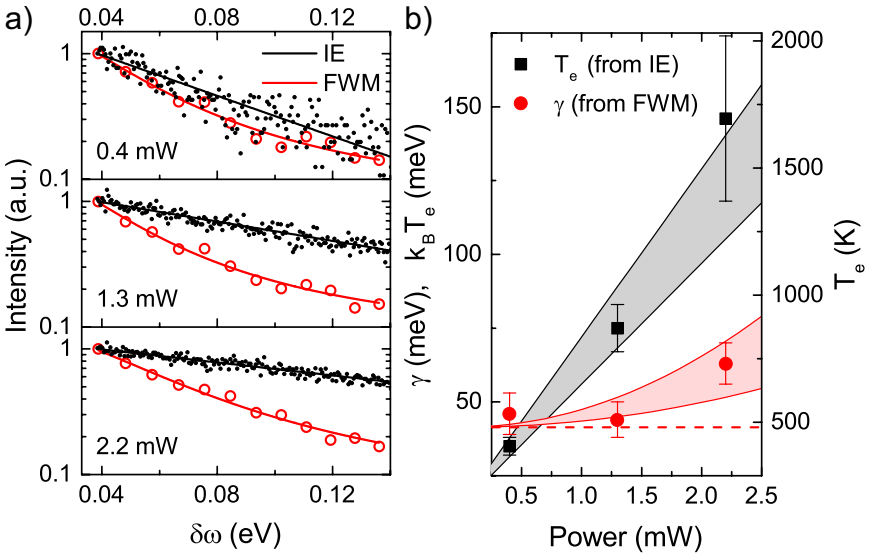

FIG. 4. (a) FWM efficiency (red) and incoherent emission (IE) background spectra (black) for excitation power, varying from 0.4 mW (top panel), to 1.3 mW (middle), and to 2.2 mW (bottom). (b) Electron gas temperature T_e (black squares) extracted from IE fits, and electron collision rate γ (red circles) extracted from FWM fits, for varying excitation power.

mechanism of the incoherent emission in Au is still under debate [35, 43–45], it generally involves electronic transitions within the *sp*-band, and therefore its spectrum depends sensitively on the temperature-dependent shape of the Fermi–Dirac distribution for the electron gas. In agreement with previous work [34, 35, 43], we can approximately describe the spectra by a Boltzmann distribution $I_{\mathrm{IE}}(\delta\omega) \propto e^{-\delta\omega/k_B T_e}$, with the electron temperature T_e increasing from 410 ± 30 K to 1700 ± 300 K for excitation powers between 0.4 mW and 2.2 mW. The extracted electron temperature is shown in Fig. 4b (black squares) together with an error-weighted linear fit, where the gray area indicates the uncertainty of the fit.

In contrast, the spectral shape of the FWM signal changes only slightly, which is consistent with our model that predicts the FWM dependence on detuning to be fully defined by only (i) spatial extent of the field gradients and (ii) electron collision rate γ. The former is defined by the tip apex geometry and therefore does not depend on excitation power. The latter is only weakly dependent on temperature for the range of laser intensities used (Fig. 4b, red circles), with only a slight increase from 46 ± 6 meV to 64 ± 7 meV. This can be attributed to temperature-dependent electron–phonon ($\gamma_{\mathrm{e-ph}}$) or electron–electron ($\gamma_{\mathrm{e-e}}$) scattering that both contribute [46, 47] to the total relaxation rate $\gamma = \gamma_{\mathrm{e-ph}} + \gamma_{\mathrm{e-e}}$. While the electron–phonon scattering rate depends on lattice

temperature that will not vary significantly during the pulse duration of < 100 fs, the electron–electron scattering rate follows the electron temperature as $\gamma_{\mathrm{e-e}} \propto (k_B T_e)^2 + (\hbar\omega)^2$. Considering the approximately linear power dependence of T_e, the corresponding power dependence of the relaxation rate can be described by a quadratic function $\gamma(P) = \gamma_0 + \alpha P^2$ (red curves, error-weighted fit), with the extracted temperature-independent contribution of $\gamma_0 = 41 \pm 6$ meV as the Drude relaxation at 0 K.

As described in this work, the enhancement of the optical nonlinearity in nanotips and nanorods through a strong dipole-forbidden third-order contribution represents a general mechanism for nano-structured media with free carriers where high field gradients can be achieved. Relying on longitudinal field gradients of plasmon modes, our mechanism complements nonlinear processes that arise from retardation-induced symmetry breaking, e.g., in second-order light scattering [29–32]. In contrast to conventional approaches for increased nonlinearity in metallic nano-particles relying on extrinsic local field enhancement, this gradient-field effect modifies the microscopic nonlinear susceptibility, and can therefore contribute even in the absence of intrinsic optical nonlinearities of the medium. Further, it provides enhancement in materials that already possess intrinsic nonlinearities, e.g., in graphene, where the strong third-order susceptibility has received much attention recently [48], yet with monolayer volume offering small signal levels that can now be increased further through nano-structuring and engineering large field gradients. With $1/R^{n-1}$ size scaling (Eq. 3) of the gradient-field term in the n-order susceptibility $\chi^{(n)}$, its contribution increases favorably with decreasing sample volume and increasing order of the nonlinearity. The results of this work not only offer insight into the microscopic mechanisms of the nonlinear optical response on the nanoscale through the hydrodynamic plasma model, but also demonstrate a qualitatively new approach to nonlinear nano-optics opening new avenues from on-chip nonlinear all-optical information processing to coherent multidimensional nano-spectroscopy and -imaging.

ACKNOWLEDGMENTS

We acknowledge funding from the National Science Foundation (NSF Grant CHE 1709822). A.B. and M.R. also acknowledge support from the Air Force Office for Scientific Research through grants FA9550-17-1-0341 and FA9550-14-1-0376. R.U. acknowledges support by a Rubicon

Grant of the Netherlands Organization for Scientific Research (NWO).

---

[1] Moss, D. J., Morandotti, R., Gaeta, A. L. & Lipson, M. New CMOS-compatible platforms based on silicon nitride and Hydex for nonlinear optics. *Nat. Photonics* **7**, 597–607 (2013).

[2] Segal, N., Keren-Zur, S., Hendler, N. & Ellenbogen, T. Controlling light with metamaterial-based nonlinear photonic crystals. *Nat. Photonics* **9**, 180–184 (2015).

[3] Lepeshkin, N. N., Schweinsberg, A., Piredda, G., Bennink, R. S. & Boyd, R. W. Enhanced nonlinear optical response of one-dimensional metal-dielectric photonic crystals. *Phys. Rev. Lett.* **93**, 123902 (2004).

[4] Lapine, M., Shadrivov, I. V. & Kivshar, Y. S. Colloquium: nonlinear metamaterials. *Rev. Mod. Phys.* **86**, 1093 (2014).

[5] Lin, H.-B. & Campillo, A. CW nonlinear optics in droplet microcavities displaying enhanced gain. *Phys. Rev. Lett.* **73**, 2440 (1994).

[6] Monat, C., De Sterke, M. & Eggleton, B. Slow light enhanced nonlinear optics in periodic structures. *J. Opt.* **12**, 104003 (2010).

[7] Kauranen, M. & Zayats, A. V. Nonlinear plasmonics. *Nature Photon.* **6**, 737–748 (2012).

[8] MacDonald, K. F., Samson, Z. L., Stockman, M. I. & Zheludev, N. I. Ultrafast active plasmonics. *Nature Photon.* **3**, 55–58 (2009).

[9] Jonas, D. M. Two-dimensional femtosecond spectroscopy. *Annu. Rev. Phys. Chem.* **54**, 425–463 (2003).

[10] Kravtsov, V., Ulbricht, R., Atkin, J. & Raschke, M. B. Plasmonic nanofocused four-wave mixing for femtosecond near-field imaging. *Nat. Nanotechnol.* **11**, 459 (2016).

[11] Tomita, K., Kojima, Y. & Kannari, F. Selective coherent anti-stokes raman scattering microscopy employing dual-wavelength nanofocused ultrafast plasmon pulses. *Nano Lett.* (2018).

[12] Zhang, Y. *et al.* Coherent anti-Stokes Raman scattering with single-molecule sensitivity using a plasmonic Fano resonance. *Nat. Commun.* **5**, 4424 (2014).

[13] Yampolsky, S. *et al.* Seeing a single molecule vibrate through time-resolved coherent anti-Stokes Raman scattering. *Nature Photon.* **8**, 650–656 (2014).

[14] Danckwerts, M. & Novotny, L. Optical frequency mixing at coupled gold nanoparticles. *Phys. Rev. Lett.* **98**, 026104 (2007).

[15] Kim, H., Taggart, D. K., Xiang, C., Penner, R. M. & Potma, E. O. Spatial control of coherent anti-stokes emission with height-modulated gold zig-zag nanowires. *Nano Lett.* **8**, 2373–2377 (2008).

[16] Palomba, S. & Novotny, L. Near-field imaging with a localized nonlinear light source. *Nano Lett.* **9**, 3801–3804 (2009).

[17] Jung, Y., Chen, H., Tong, L. & Cheng, J.-X. Imaging gold nanorods by plasmon-resonance-enhanced four wave mixing. *J. Phys. Chem. C* **113**, 2657–2663 (2009).

[18] Genevet, P. *et al.* Large enhancement of nonlinear optical phenomena by plasmonic nanocavity gratings. *Nano Lett.* **10**, 4880–4883 (2010).

[19] Lippitz, M., van Dijk, M. A. & Orrit, M. Third-harmonic generation from single gold nanoparticles. *Nano Lett.* **5**, 799–802 (2005).

[20] Knittel, V. *et al.* Dispersion of the nonlinear susceptibility in gold nanoantennas. *Phys. Rev. B* **96**, 125428 (2017).

[21] Payne, L. *et al.* Optical micro-spectroscopy of single metallic nanoparticles: quantitative extinction and transient resonant four-wave mixing. *Faraday Discuss.* **184**, 305–320 (2015).

[22] Zoriniants, G., Masia, F., Giannakopoulou, N., Langbein, W. & Borri, P. Background-free 3d nanometric localization and sub-nm asymmetry detection of single plasmonic nanoparticles by four-wave mixing interferometry with optical vortices. *Phys. Rev. X* **7**, 041022 (2017).

[23] Cox, J. D., Marini, A. & De Abajo, F. J. G. Plasmon-assisted high-harmonic generation in graphene. *Nat. Commun.* **8**, 14380 (2017).

[24] Hache, F., Ricard, D. & Flytzanis, C. Optical nonlinearities of small metal particles - surface-mediated resonance and quantum size effects. *J. Opt. Soc. Am. B* **3**, 1647–1655 (1986).

[25] Hache, F., Ricard, D., Flytzanis, C. & Kreibig, U. The optical kerr effect in small metal particles and metal colloids: the case of gold. *Appl. Phys. A* **47**, 347–357 (1988).

[26] Lysenko, O., Bache, M., Olivier, N., Zayats, A. V. & Lavrinenko, A. Nonlinear dynamics of ultrashort long-range surface plasmon polariton pulses in gold strip waveguides. *ACS Photonics* **3**, 2324–2329 (2016).

[27] Palomba, S. & Novotny, L. Nonlinear excitation of surface plasmon polaritons by four-wave mixing. *Phys. Rev. Lett.* **101**, 056802 (2008).

[28] Ginzburg, P., Hayat, A., Berkovitch, N. & Orenstein, M. Nonlocal ponderomotive nonlinearity in plasmonics. *Opt. Lett.* **35**, 1551–1553 (2010).

[29] Dadap, J. I., Shan, J., Eisenthal, K. B. & Heinz, T. F. Second-harmonic Rayleigh scattering from a

sphere of centrosymmetric material. *Phys. Rev. Lett.* **83**, 4045 (1999).

[30] Neacsu, C., Reider, G. & Raschke, M. Second-harmonic generation from nanoscopic metal tips: Symmetry selection rules for single asymmetric nanostructures. *Phys. Rev. B* **71**, 201402 (2005).

[31] Roke, S., Bonn, M. & Petukhov, A. V. Nonlinear optical scattering: The concept of effective susceptibility. *Phys. Rev. B* **70**, 115106 (2004).

[32] Dadap, J. I., de Aguiar, H. B. & Roke, S. Nonlinear light scattering from clusters and single particles. *J. Chem. Phys.* **130**, 214710 (2009).

[33] Berweger, S., Atkin, J. M., Xu, X. G., Olmon, R. L. & Raschke, M. B. Femtosecond nanofocusing with full optical waveform control. *Nano Lett.* **11**, 4309–4313 (2011).

[34] Huang, J. Y., Wang, W., Murphy, C. J. & Cahill, D. G. Resonant secondary light emission from plasmonic Au nanostructures at high electron temperatures created by pulsed-laser excitation. *Proc. Natl. Acad. Sci. U.S.A.* **111**, 906–911 (2014).

[35] Haug, T., Klemm, P., Bange, S. & Lupton, J. M. Hot-electron intraband luminescence from single hot spots in noble-metal nanoparticle films. *Phys. Rev. Lett.* **115**, 067403 (2015).

[36] Hu, Q. *et al.* Position-sensitive spectral splitting with a plasmonic nanowire on silicon chip. *Sci. Rep.* **3**, 3095 (2013).

[37] Boyd, R. W., Shi, Z. & De Leon, I. The third-order nonlinear optical susceptibility of gold. *Opt. Commun.* **326**, 74–79 (2014).

[38] Rotenberg, N., Bristow, A., Pfeiffer, M., Betz, M. & Van Driel, H. Nonlinear absorption in Au films: Role of thermal effects. *Phys. Rev. B* **75**, 155426 (2007).

[39] Neacsu, C. C. *et al.* Near-field localization in plasmonic superfocusing: a nanoemitter on a tip. *Nano Lett.* **10**, 592–596 (2010).

[40] Johnson, P. & Christy, R. Optical constants of the noble metals. *Phys. Rev. B* **6**, 4370 (1972).

[41] Olmon, R. L. *et al.* Optical dielectric function of gold. *Phys. Rev. B* **86**, 235147 (2012).

[42] Renger, J., Quidant, R., Van Hulst, N. & Novotny, L. Surface-enhanced nonlinear four-wave mixing. *Phys. Rev. Lett.* **104**, 046803 (2010).

[43] Hugall, J. T. & Baumberg, J. J. Demonstrating photoluminescence from Au is electronic inelastic light scattering of a plasmonic metal: the origin of SERS backgrounds. *Nano Lett.* **15**, 2600–2604 (2015).

[44] Lin, K. Q. *et al.* Intraband hot-electron photoluminescence from single silver nanorods. *ACS Photonics* **3**, 1248–1255 (2016).

[45] Mertens, J., Kleemann, M.-E., Chikkaraddy, R., Narang, P. & Baumberg, J. J. How light is emitted by

plasmonic metals. *Nano Lett.* **17**, 2568–2574 (2017).

[46] Link, S. & El-Sayed, M. A. Size and temperature dependence of the plasmon absorption of colloidal gold nanoparticles. *J. Phys. Chem. B* **103**, 4212–4217 (1999).

[47] Liu, M., Pelton, M. & Guyot-Sionnest, P. Reduced damping of surface plasmons at low temperatures. *Phys. Rev. B* **79**, 035418 (2009).

[48] Glazov, M. & Ganichev, S. High frequency electric field induced nonlinear effects in graphene. *Phys. Rep.* **535**, 101–138 (2014).